

1 **What fraction of the outer radiation belt relativistic electron flux at $L \approx 3-4.5$ was lost to the**
2 **atmosphere during the dropout event of the St Patrick's Day storm of 2015?**

3 Sneha Gokani^{1,2*}, Mike Kosch^{3,4,5}, Mark Clilverd⁶, Craig J. Rodger⁷, and Ashwini K. Sinha¹

4
5 ¹ Indian Institute of Geomagnetism, New Panvel, Navi Mumbai – 410218, India

6 ² State Key Laboratory of Marine Geology, School of Ocean and Earth Science, Tongji
7 University, Shanghai-200092, China

8 ³ South African National Space Agency, Hospital Street, PO Box 32, Hermanus, 7200, South
9 Africa

10 ⁴ Department of Physics, Lancaster University, Lancaster, LA1 4YB, UK

11 ⁵ Department of Physics and Astronomy, University of Western Cape, Bellville 7535, South
12 Africa.

13 ⁶ British Antarctic Survey (UKRI-NERC), High Cross, Madingley Road, Cambridge, CB3 0ET

14 ⁷ Department of Physics, University of Otago, PO Box 56, Dunedin 9054, New Zealand

15

16

17 *Corresponding author: Sneha A. Gokani (gokanisneha@gmail.com)

18

19

20

21 **Key Points:**

22 • A dropout event during the 2015 St. Patrick's Day storm is examined to find the electron
23 flux lost to the atmosphere

24 • Clear perturbations in VLF signal amplitude and phase are seen at $L \approx 3-4.5$ at the time of
25 the dropout event

26 • Less than $\sim 0.5\%$ of the relativistic flux lost at $L \approx 4$ during the dropout was due to
27 precipitation into the atmosphere

28

29 **Abstract**

30 Observations of relativistic energetic electron fluxes in the outer radiation belt can show
31 dropouts, i.e., sudden electron flux depletions during the main phase of a geomagnetic storm.
32 Many recent studies show that these dropouts typically involve a true loss of particles i.e. non-
33 adiabatic losses in nature. Precipitation into the atmosphere of relativistic electrons driven into
34 the bounce loss cone, through wave particle interactions, is envisaged as one of the primary loss
35 mechanisms. Such precipitation can be studied using ground based observations such as VLF
36 narrow-band radio waves, due to the deposition of energy into the lower ionospheric D-region,
37 thereby modifying the sub-ionospheric waveguide. The present study focuses on the dropout
38 event observed during the St. Patrick's Day storm of March 2015. Perturbations lasting several
39 hours were observed in the received VLF amplitude and phase of the NAA transmitter signal
40 measured at Seattle and Edmonton, and the NML transmitter signal received at St. John's and
41 Edmonton. All these $L \approx 3-4.5$ paths were located on the night-side of the Earth during dropout
42 phase of the storm. Observations of relativistic electron characteristics from Van Allen Probes,
43 and ionospheric perturbation characterization from VLF radio waves, are used to calculate that
44 during the time interval of the dropout event $<0.5\%$ of the relativistic fluxes involved in the
45 dropout event were lost to the atmosphere. This leads to the conclusion that relativistic electron
46 precipitation was not the major contributor to the observed dropout event at $L \approx 4$ that occurred
47 during the St. Patrick's Day storm of March 2015.

48

49

50 **Key words:** Radiation belt dropout, VLF transmitter, Radiation belts, Relativistic electron loss

51 **1. Introduction**

52 The radiation belts are formed as a consequence of trapping of charged particles by
53 Earth's magnetic field. Populated by energetic electrons and protons, these belts are distributed
54 in two distinct toroidal zones known as, 'inner' and 'outer' belts, separated by a slot region. The
55 relatively stable inner belt is centred on $L \approx 1.4$ and extends up to about $L \approx 2$ with electrons having
56 characteristic energy levels of a few tens of keV. The dynamic outer belt is centred on $L \approx 4$ and
57 extends from $L \approx 3$ to 6 with electrons having characteristic energies of 100's of keV to a few
58 MeV. The slot region ($L \approx 2-2.5$) is thought to be the result of energetic electron precipitation
59 losses through wave-particle interactions (Lyons and Thorne, 1973; Kivelson and Russell, 1995).
60 Though radiation belt physics have been studied from the beginning of the Space Era, the launch
61 of NASA's Van Allen Probes mission gained much attention as it was dedicated to develop
62 much deeper understanding of radiation belt structure and dynamics (Mauk et al., 2012). Since
63 their launch in 2012, the Van Allen Probes have provided the most comprehensive in-situ
64 measurements to date.

65 The structure and variability of electron fluxes in the outer radiation belt is believed to be
66 controlled by the competition between source and loss processes (Millan and Thorne, 2007),
67 which can alter greatly during intense geomagnetic activity (Ukhorskiy et al., 2006; Bortnik et
68 al., 2006; Turner et al., 2014; Herrera et al., 2016; Zhang et al., 2016). However, the net increase
69 or decrease of outer belt electron flux is decided by a delicate balance between particle
70 acceleration and loss (Reeves et al, 2003). These source, loss, and transport processes show
71 temporal and spatial variations depending upon the complex plasma conditions that are driven by
72 the solar wind and the interplanetary magnetic field. The radiation belt source process is often
73 manifested by the acceleration of electrons in the outer belt. This acceleration can sometimes be

74 provided by inward radial diffusion (Schulz and Lanzerotti, 1974). It is also proposed that when
75 ~100 keV electrons interact with whistler-mode chorus waves they can be accelerated to ~MeV
76 energies (Summers et al., 1998; Horne and Thorne, 1998; Miyoshi et al., 2003; Horne et al.,
77 2005; Li et al., 2007; Reeves et al., 2013; Thorne et al., 2013; Boyd et al., 2014). On the other
78 hand, the loss of energetic electrons is typically attributed to three possible mechanisms: (i)
79 adiabatic motion (ii) magnetopause shadowing and (iii) precipitation into the atmosphere (Green
80 et al., 2004).

81 The adiabatic electron losses are reversible in a sense that the particles are redistributed
82 radially to conserve three adiabatic invariants (Dessler and Karplus, 1960; McIlwain, 1966). The
83 increased ring current intensity during storm main phase decreases the magnetic flux, due to
84 which the electrons are compelled to decelerate and move outward in order to conserve the first
85 and third adiabatic invariants respectively (Ukhorskiy et al., 2006; Boynton et al., 2016). This
86 energetic electron flux returns to approximately the same location and energy once the ring
87 current recovers after the storm (Kim and Chan, 1997).

88 Losses to the outer boundary, i.e., the magnetopause, can occur when the magnetopause
89 is displaced inward by increased solar wind pressure during a geomagnetic storm. Due to this,
90 the electrons find themselves on open drift shells and can be lost to interplanetary space (Bortnik
91 et al., 2006; Kim et al., 2008; Herrera et al., 2016). This effect is known as ‘magnetopause
92 shadowing’ (West et al., 1973).

93 Precipitation into the atmosphere can occur through resonant wave-particle interactions
94 which decrease the electron’s pitch angle. A variety of plasma waves have been identified,
95 depending upon the region, time and energy of the particles, that drive pitch angle scattering into
96 the drift and bounce loss cone (Bortnik et al., 2006). This includes electromagnetic ion cyclotron

97 waves (EMIC) (Thorne et al., 2005; Miyoshi et al., 2008; Clilverd et al., 2015), plasmaspheric
98 ELF/VLF hiss (Lyons and Thorne, 1973), high latitude VLF chorus (Behra et al., 2017) and
99 Electron Cyclotron Harmonic (ECH) waves (Ni et al., 2012).

100 EMIC waves are pulsations in Pc1-2 having frequencies below proton gyrofrequency.
101 These waves are generated near the field-line magnetic equator (Fraser et al., 1996; Loto'aniu et
102 al., 2005) by unstable ion distributions in the ring current (Cornwall, 1965; Anderson et al.,
103 1993). The waves can grow when strong temperature anisotropy exists ($T_{perp.} > T_{par.}$) (Kozyra et
104 al., 1984). The largest amplitude waves are seen in the dusk and dayside sectors at high L-shells
105 ($L > 5$) and the occurrence rate is found to increase by up to a factor of five during major
106 geomagnetic storms (Erlandson and Ukhorskiy, 2001). 'Anomalous' gyro-resonance between an
107 electron and EMIC wave occurs when an electron overtakes a wave (Thorne and Kennel, 1971)
108 so as to change the apparent polarization of the wave in the frame of electron. The typical
109 resonant energies are > 10 MeV in lower density regions outside the plasmasphere and can drop
110 to ≤ 1 MeV in regions like the plasmopause and in plasmaspheric plumes where the cold plasma
111 electron density is relatively high (Thorne and Kennel, 1971; Meredith et al., 2003; Summers
112 and Thorne, 2003; Ukhorsky et al., 2010).

113 Plasmaspheric hiss is a broadband (~ 100 Hz - few kHz) VLF emission generated in the
114 equatorial plane by the electron-cyclotron instabilities (Thorne et al., 1973). These waves are
115 found in high density regions like the plasmasphere and plasmaspheric plumes. The highest
116 amplitude waves are found in the dawn to evening sector. These waves allow resonance with
117 \sim MeV electrons below $L \sim 3$ (Thorne et al., 1979).

118 Whistler-mode chorus waves are discrete emissions in the frequency range of ~ 100 Hz –
119 5 kHz (Sazhin and Hayakawa, 1992) resulting from cyclotron instabilities (Kennel and Petschek,

120 1966) occurring near the geomagnetic equator in association with freshly injected plasma sheet
121 electrons (Tsurutani and Smith, 1974). The chorus intensity increases during substorm activity
122 and during the recovery phase of storms (Meredith et al., 2001; Li et al., 2009). Chorus waves,
123 depending upon the electron energies, can accelerate or scatter these particles into the loss cone.
124 The chorus wave can interact with 100 keV electrons in the ring current and outer radiation belt
125 to accelerate the electrons to MeV energies (Temerin et al., 1994; Horne and Thorne, 1998;
126 Summers et al., 1998).

127 The non-adiabatic loss processes of magnetopause shadowing, and electron precipitation
128 are the ‘true’ losses of energetic electrons. Precipitation by resonant wave-particle interaction,
129 depends on particle energies, particle pitch angles, L-shells, plasma wave modes, frequencies and
130 intensities under different interplanetary and magnetospheric conditions (Tsurutani et al., 2016).
131 The losses of energetic electron fluxes at the start of geomagnetic storm events are known as
132 ‘dropouts’ and are often rapid, i.e., the flux can decrease by several orders of magnitude in a few
133 hours. These dropout events are also defined as a flux decrease by factor of 4 in a day or a factor
134 of 9 in two days where the decrease should account for at least a factor of 2.5 each day (Boynton
135 et al., 2016). These sudden fluctuations in the flux are attributed to above mentioned loss
136 mechanisms, but the relative dominance of each mechanism likely varies from event to event.

137 Recently Shprits et al. (2017) have postulated that EMIC waves have the potential to
138 precipitate relativistic electrons (2-6 MeV) from the outer radiation belt on rapid timescales, and
139 may be the dominant factor in the generation of radiation belt dropout events. Traditionally
140 EMIC waves are expected to precipitate electrons >1 MeV (Thorne and Kennel, 1971) although
141 in the last few years studies have shown that some EMIC waves can induce electron precipitation
142 with energies of >200 keV (Hendry et al., 2017). There are very few studies on the estimation of

143 the flux loss during dropouts as a result of relativistic electron precipitation. Recently, Zhang et
144 al. (2017) estimated a net loss up to 6.8% of the 0.58-1.63 MeV electrons in a precipitation band
145 event using conjunctive measurement of the Colorado Student Space Weather Experiment
146 (CSSWE) mission, the Balloon Array for Radiation belt Relativistic Electron Losses (BARREL),
147 and one of the Polar Operational Environmental Satellites (POES). Previous analysis of non-
148 relativistic electron precipitation (typically 30 keV -1 MeV) using the NOAA POES satellites
149 have shown that electron precipitation occurs typically 3 hours after the dropout, and not during
150 it (Hendry et al., 2012). The non-relativistic precipitation appears to more likely to be linked to
151 the period where the outer radiation belt electron fluxes are recovering as a result of acceleration
152 processes.

153 It is unclear what fraction of the outer radiation belt flux is lost during dropout events
154 through electron precipitation mechanisms. Baker et al. (2016) have speculated that the dropout
155 of >1 MeV electrons on 17 March 2015 was due to magnetopause shadowing. However,
156 radiation belt models have been found to under-estimate the flux lost when applying only
157 magnetopause shadowing effects to their simulations (Glauert et al., 2018). In this paper, we use
158 ground-based subionospheric radiowave propagation observations to investigate the dropout
159 event that occurred at ~06 UT on 17 March 2015 during the St. Patrick's Day storm. The dropout
160 in relativistic electron flux levels was observed by the Van Allen Probes satellites. The focus of
161 this work is to estimate the amount of relativistic electron flux precipitating into the atmosphere
162 during the event, using ground based subionospheric VLF receiver data. Rodger et.al. (2011) has
163 investigated the sensitivity of subionospheric VLF paths in the north American region by
164 applying excess ionization generated by mono-energetic beams of precipitating electrons and
165 power law spectrum, to the D-region during daytime and nighttime conditions. Their results

166 show that the precipitation of >300 keV electrons exhibit large VLF amplitude and phase
167 variations, and the technique is more sensitive during night as compared to daytime. The aim of
168 this study is to investigate what fraction of the radiation belt relativistic electron flux has
169 precipitated in to the atmosphere so as to cause the observed VLF signal perturbations at $L \approx 3$ -
170 4.5. Section 2 describes the event and datasets available. Section 3 describes the satellite [3.1]
171 and ground based observations [3.2] prior to, and during, the dropout event. Section 4.1 models
172 the electron density that reproduces the observed VLF perturbations during the dropout event.
173 Section 4.2 determines the characteristics of the electron precipitation observed from the Van
174 Allen Probes, and compares them to those found in section 4.1 in order to determine the potential
175 flux of precipitating relativistic electrons. Finally, section 5 estimates the fraction of trapped
176 relativistic electron flux lost to the atmosphere during the dropout event.

177 **2. Experimental Setup and Data**

178 The solar cycle 24 started dramatically in 2009 after prolonged minima from 2006-2008.
179 Surprisingly, there was not much geomagnetic activity even during the peak of the cycle until the
180 first super geomagnetic storm in the declining phase of the cycle, on St. Patrick's day of 2015
181 with $Dst = -223$ nT. The two step storm is thought to have been initiated by a halo coronal mass
182 ejection (CME), erupted from the Sun on 15 March 2015 (Wu et al., 2016). Figure 1 represents
183 the interplanetary (IP) conditions on 17 March 2015. There is no data gap in ACE level 2 data
184 but there is a data gap from ~ 7 -9 UT in the processed OMNI data. The Wind spacecraft recorded
185 an IP shock at 03:57 UT on the event day and the arrival of the shock at the Earth produced a
186 sudden storm commencement (SSC) at 04:45 UT, represented by the vertical black line. The
187 solar wind speed at that time showed an increase from ~ 400 km/s to ~ 500 km/s. Initially the IMF
188 B_z was northward until 05:00 UT and then turned southward to give $B_z \sim -20$ nT which decreased

189 further as the storm progressed and the solar wind speed increased to its maximum value of ~600
190 km/s. The main phase of the storm lasted about 18 hrs from ~6-23 UT on 17 March 2015.

191 To investigate the energetic electron precipitation into the atmosphere, narrowband VLF
192 transmitter signals from NAA (44.6° N, 67.3°W) operating at a frequency of 24.0 kHz received
193 at Seattle (47.9° N, 124.4°W) and Edmonton (53.35° N, 112.97° W) and the transmitter signals
194 from NML (46.4° N, 98.3°W) operating at a frequency of 25.2 kHz received at St. John's (47.6°
195 N, 52.7°W) and Edmonton, are used. The great circle path lengths for NAA-Seattle is ~4305 km,
196 NAA-Edmonton is ~3406 km, NML-St. John's is ~3410 km and NML-Edmonton is ~1301 km
197 respectively. These transmitters and receivers are the part of the AARDDVARK Network
198 (Clilverd et al., 2009). More information about the network can be found at
199 http://www.physics.otago.ac.nz/space/AARDDVARK_homepage.htm. Figure 2 shows the
200 transmitter-receiver sites with great circle paths (GCP) and L = 3, 4, 5 contours. The sub-
201 ionospheric propagation paths are predominantly orientated east-west, and can be used to
202 remotely sense electron precipitation events at quasi-constant geomagnetic latitudes of $L\sim 3-4.5$.

203 Some indication of the dynamic behaviour of relativistic electron fluxes in the outer
204 radiation belt during the main phase of the March 2015 storm can be determined from the POES
205 SEM-2 telescope P6 (see Rodger et al., 2010 for a description of the instrument). Figure 3 shows
206 the P6 trapped (upper panel) and bounce-loss-cone precipitating fluxes (lower panel) from all
207 available POES observations during 17 March 2015. The colour scale represents the logarithm
208 of the flux levels. The vertical dashed lines represent the dropout period that will be investigated
209 in this paper, i.e., 06:30 to 08:30 UT, while the purple box represents the L-shell ranges for
210 which VLF sub-ionospheric narrow-band data described in the paragraph above, and are
211 analysed during the storm period. In the absence of solar protons the P6 telescope responds to

212 electrons with energy >700 keV (Yando et al., 2011) and thus the figure indicates that relativistic
213 trapped fluxes reduced over the L-shell range 3.5 to 5.5 at 06:30 UT (upper panel), while the
214 only observable relativistic electron precipitation into the atmosphere occurred between 06:30
215 and 08:30 UT, and in the L=3.5 to 4.0 range (lower panel). We show the POES P6 channel as it
216 is a direct measure of the electron precipitation flux relevant to the electron energies involved in
217 relativistic electron flux dropouts (Baker et al., 2016) that are investigated in this paper, i.e.,
218 >700 keV. The L-shell range over which the subionospheric VLF analysis will be performed in
219 this study is well suited to investigate these regions. While the POES P6 telescope observed clear
220 electron precipitation signatures at the time of the radiation belt dropout the geometric factor of
221 the P6 detector for electron ‘contamination’ is complex and does not allow clear identification of
222 the electron energies involved, or what their flux levels might be. In order to investigate this
223 event in more detail we turn to the Van Allen Probes mission and its energetic electron
224 telescopes.

225 The dropout in radiation belt energetic electron flux on 17 March 2015 was seen by the
226 Relativistic Electron-Proton Telescope (REPT, \sim MeV electrons) with supporting information
227 provided by the Magnetic Electron Ion Spectrometer (MagEIS, \sim keV electrons) instruments on
228 board the Van Allen Probes (Popularly known as RBSP). The RBSP consist of two probes, A
229 and B, placed in very close orbits to study the events that occur simultaneously throughout the
230 belts or localized at a point or which evolve with time from one point to another. The spacecraft
231 have nearly elliptical orbits lying in Earth's equatorial plane with $\sim 20^\circ$ inclination. The REPT
232 and MagEIS form part of the Energetic Particle, Composition, and Thermal Plasma Suite (ECT)
233 which is dedicated to the measurement of particle energy and pitch angle. The REPT instrument
234 measures the particles with relativistic energies, binned in 12 energy bands from 1.8 MeV – 20

235 MeV. The MagEIS instrument measures the particles with lower energies, ranging from 31.5
236 keV – 4.2 MeV, distributed in 21 bins.

237 **3. Observations**

238 **3.1 RBSP Energetic Electron Flux Observations**

239 The ionospheric footprints of RBSP-A at time $t_1 = 06:30$ UT and $t_2 = 08:30$ UT are
240 located at $\sim 164.4^\circ$ E and $\sim 158.3^\circ$ W, and that of RBSP-B are at $\sim 117.6^\circ$ W and $\sim 124.5^\circ$ W
241 respectively as shown in Figure 2. A deep ‘dropout’ of electrons with energies in the range 2.0-
242 4.2 MeV was observed by REPT as shown in Figure 4 (panels a - f) during the main phase of the
243 storm. Equivalent MagEIS observations are shown in Figure 4 (panels g - l). Figure 4 (panels a -
244 c) represents the color coded spin averaged intensities of REPT electrons with energies ~ 2.0
245 MeV, ~ 3.6 MeV and ~ 4.2 MeV for March 2015. Figure 4 (panels d - f) are the zoomed views of
246 panels a - c providing a closer look at two days around the time of the dropout that started at
247 $\sim 06:30$ UT on 17 March. The flux decrease can be clearly seen from $L=3.5$ to 6 in each energy
248 range, but we restrict this study of the dropout at $L\sim 4$ as the VLF perturbations are observed over
249 $L\sim 3$ to 4.5. The black vertical lines in the figure represent the duration of observed VLF
250 perturbations as discussed later in this section, and we will focus on this time period throughout
251 our further analysis in order to investigate the cause of the observed VLF perturbations.

252 The 2.0 MeV flux started to recover around 16:00 UT on 17 March 2015 whereas the
253 higher energy flux (~ 4.2 MeV) did not recover until the early hours of 18 March 2015,
254 coinciding with the main phase of the storm as mentioned in section 2. Figure 4 (panels g - i)
255 shows the same format as panels a – c, but for MagEIS electrons of energies ~ 221 , ~ 464 and
256 ~ 741 keV respectively, while panels j-l provide a zoomed view of the same energy channels

257 around the event time. There is no RBSP-A data available for ~221 keV channel. Although
258 enhancements in the MagEIS electron energies are observed as a result of the St Patrick's day
259 storm, there is no clear dropout event at energies of 226 keV, a dropout is seen for 464 keV at
260 $L \approx 5$, while the 741 keV observations suggest that there is a small decrease in flux at the time of
261 the dropout in already low flux levels occurring in the preceding days. Detailed inspection of the
262 REPT and MagEIS channels suggest that the dropout in flux on 17 March 2015 is clearly
263 discernible from $L=3.5-6$ over energy ranges from 900 keV to 6.3 MeV. Based on the Van Allen
264 Probes observations of those energy channels showing decreased flux levels during the dropout
265 event, for the remainder of this study we take the energy range of the EEP to span 900-6300keV.

266 In order to determine the potential percentage of the total tube flux that could have been
267 lost to the atmosphere during the flux dropout event it is important to be able to determine the
268 pitch angle distribution (α) at each energy in order to estimate the total tube content. It is also
269 important to know the energy spectra of the precipitating flux in the bounce loss cone in order to
270 be able to estimate the flux that produces the VLF perturbations - for this we use pitch angle
271 information as close to the bounce loss cone as possible. Figure 5 (panels a – e) represents the
272 MagEIS pitch angle distribution for 2.0, 2.25, 2.85, 3.6 and 4.5 MeV electrons observed at 07:41
273 UT, 17 March 2015, as RBSP-A passed through the $L=4$ flux tube, close to the magnetic field
274 line equator. The timing is close to the start of the observed dropout event as shown in Figure 4.
275 The pitch angle variation is given by a sinusoidal curve with $\sin^n \alpha$, where n takes values from 1
276 to 3 for 2.0 to 4.5 MeV, respectively, shown by a solid red curve in the Figure. We also plot
277 particle flux as a function of energy at 90° and 15° pitch angles (panel f). From the power law fit,
278 it is seen that the power law gradient is -7.7 for 90° pitch angles while it is -8.8 nearer to bounce
279 loss cone ($\sim 6^\circ$ at $L=4$) i.e., at 15° pitch angles. The next time that RBSP-A crossed the $L=4$ field

280 line was at 13:18 UT, which was close to the end of the observable dropout period, and showed
281 95-98% reductions in relativistic flux levels. These values will be used as an input to calculate
282 ionospheric impact in section 4.2 of this paper, and flux tube total content in section 5.

283 **3.2 Perturbations in narrowband VLF transmitter signals**

284 VLF narrowband transmitter signals are a good tool to study any changes in the lowest
285 region of the ionosphere that occur due to any forcing from above or below. The lower
286 ionospheric changes are reflected as an increase or decrease in amplitude and phase of
287 narrowband VLF transmitter signals. The VLF signals may incur amplitude and phase
288 perturbations due to energetic electron precipitation (Rodger et al., 2008, Clilverd et al., 2015)
289 which alters the ionospheric propagation conditions. In Figure 6 we show such subionospheric
290 VLF data on 17 March 2015. We observe clear amplitude and phase perturbations just after the
291 onset of the geomagnetic storm on 17 March 2015 in VLF transmitter signals received at Seattle
292 and Edmonton from NAA and those received at St. John's and Edmonton from the NML
293 transmitter. Figure 6 (a) shows the amplitude (left hand panels) and phase perturbations (right
294 hand panels) observed in the four paths over the whole day. The black curve is the signal on the
295 disturbed day whereas the red curve represents the quiet day curve (QDC) of the narrowband
296 VLF transmitter signal for respective paths. Asterisks represent radio wave propagation
297 modelling (Ferguson, 1998) results for non-disturbed nighttime conditions (Thomson et al.,
298 2011a; 2011b) and equivalent conditions during the day (Ferguson, 1998). Here we follow the
299 technique of Thomson et al. (2007), and Thomson and McRea (2009) who use the relative phase
300 and amplitude at night compared with the much more well known conditions during the day (as
301 they are driven by direct photoionisation) in order to determine the ambient amplitude and phase
302 levels during the pre-event (nighttime) period. Good agreement is seen between the modelling

303 results and pre-event amplitude and phase values, suggesting that non-disturbed D-region
304 profiles are a reasonable description of the pre-event conditions. The radiowave modelling will
305 be discussed further in section 4.1.

306 In all of the panels of Figure 6 (a) we made some estimates of the variability of the non-
307 disturbed amplitudes and phases in the observed values in the three hours immediately prior to
308 the dropout precipitation event. These are shown as green horizontal lines. We find that there
309 could be an uncertainty in the amplitude of ± 2.5 dB, and in phase of $\pm 50^\circ$. These uncertainty
310 limits will be taken into account in the determination of the dropout perturbation size, and in the
311 resulting estimation of the likely D-region profile that the radio wave perturbations suggest (see
312 section 4.1).

313 Figure 6 (b) represents the amplitude (left hand panels) and phase perturbations (right
314 hand panels) observed for all the four paths, NAA-Seattle, NML-St. John's, NAA-Edmonton
315 and NML-Edmonton, from 6-9 UT. The initial deviations from the respective quiet day curves in
316 both amplitude and phase for both the paths begin at ~ 6.3 UT. A sudden amplitude decrease of
317 $\sim 23 \pm 2.5$ dB and an increase in phase by $\sim 213 \pm 50^\circ$ is observed for NAA-SEA around 6.8 UT.
318 Similarly, a sudden amplitude decrease of $\sim 27 \pm 2.5$ dB and phase increase of $\sim 218 \pm 50^\circ$ is
319 observed for NML-STJ around 7 UT. The VLF signal features an average decrease of $\sim 8.5 \pm 2.5$
320 dB and $\sim 12.8 \pm 2.5$ dB over both the paths respectively during the period of almost two hours
321 from ~ 6.5 to 8.5 UT. This duration is shown by black vertical lines in the Figure 6. During this
322 period, the VLF signal showed an average phase increase of $\sim 142 \pm 50^\circ$, $\sim 172 \pm 50^\circ$, $\sim 250 \pm 50^\circ$
323 and $\sim 180 \pm 50^\circ$ for NAA-Seattle, NML-St. John's, NAA-Edmonton and NML-Edmonton paths
324 respectively, starting around ~ 6.3 UT as shown by black dashed line in lower panel of Figure 6.
325 The perturbations found in this study (10's of dB and several 100's of degrees) are of very

326 similar size to the effects seen by a large range of published event studies, a subset of which
327 include the effects of substorms (Clilverd et al., 2008, 2012), EMIC waves (Rodger et al., 2008;
328 Clilverd et al., 2015), Plasmaspheric hiss (Hardman et al., 2015), and medium-large solar flares
329 (Thomson et al., 2005). Therefore, while the perturbations during the dropout event are clear,
330 and substantial, they are consistent in size with the effects of many other relatively common
331 phenomena, and do not immediately suggest that a large portion of the radiation belt relativistic
332 flux has been lost to the atmosphere during the dropout event. However, the coincidence of VLF
333 perturbations during the main phase of the storm starting at the same time as the relativistic
334 electron dropout event provides the motivation for the current study.

335 The effects of substantial precipitation occurring on the subionospheric path between
336 Iceland and Sodankylä, Finland (L=5.5 to 6) was also seen, which shows that the MLT region
337 covered by the electron precipitation at least ranges from 00-08 MLT. In the case of the
338 observations from NRK (37.5kHz, Reykjavik, Iceland) to Sodankylä, Finland, the amplitude
339 change at ~06 UT was ~-40 dB, pushing the signal into the noise floor, and as a result the
340 AARDDVARK receiver lost phase lock. Therefore, no estimate of the electron precipitation flux
341 at L~6 could be made using those observations. We note, however, that the precipitation started
342 at 06 UT at L~6, compared with ~6.3 UT at L~3-4, suggesting a delay in response at lower L-
343 shells compared with higher L.

344 **4. Modelling Results**

345 **4.1 LWPC Modelling**

346 To infer the changes in the lower ionosphere on the event day, we first model the quiet
347 time signal using the Long Wave Propagation Capability (LWPC) v 2.1 code developed by the

348 US Naval Ocean System Center (NOSC) (Ferguson, 1998). This code calculates the full-wave
349 reflection coefficients for the waveguide boundaries by taking into account the input path
350 parameters. The process leads to the search for modal angles which give phase change of 2π
351 across the guide taking into consideration the curvature of the Earth (Morfitt and Shellman,
352 1976). The program basically determines the upper boundary of the waveguide in terms of two
353 ‘Wait parameters’ used to describe the electron number density of the lower ionosphere through
354 the sharpness factor, β (in km^{-1}) and reference height, H' (in km) (Wait and Spies, 1964). We use
355 the LWPC code to determine the electron profile characteristics of the ionosphere that would
356 have caused the VLF signal changes during the dropout event. For the undisturbed conditions
357 (i.e., without additional electron precipitation) we use $\beta = 0.3 \text{ km}^{-1}$ and $H' = 74 \text{ km}$ for daytime
358 (12 - 23 UT) and $\beta = 0.63 \text{ km}^{-1}$ and $H' = 85.1 \text{ km}$ for nighttime (0 - 11 UT) (Thomson et al.,
359 2007; 2011a; 2011b). The blue asterisks in Figure 6 represent the modelled signal. One can see
360 that the modelled signal matches the quiet day curve shown by red, and suggests that the pre-
361 event conditions are well represented by non-disturbed D-region profiles that have previously
362 been determined, and extensively published in the past.

363 To further infer the ionospheric lower boundary conditions during the dropout event of
364 17 March 2015, the amplitude and phase perturbations of the VLF signal relative to the quiet day
365 levels are plotted against H' for different values of β , for all four paths as shown in Figure 7. This
366 exercise leads to the H' and β which would cause the observed perturbation in the VLF signal.
367 The left panels show the amplitude and phase perturbations for the NAA-SEA and NAA-EDM
368 subionospheric propagation paths; while the right panels show the equivalent results for the
369 NML-STJ and NML-EDM propagation paths. The horizontal dot-dashed lines represent the
370 experimentally observed changes in amplitude and phase on 17 March 2015 for each path, as

371 mentioned in section 3.2. The vertical black line indicates the solution for H' that best matches
372 the observed perturbation levels on the four paths. The green square centred on the crossing point
373 of the two lines represents the upper and lower limits of the uncertainty in the perturbation levels
374 due to uncertainty in the pre-event levels, as shown in Figure 6, and identifies the H' range that is
375 necessary to take in to account the perturbation uncertainty. It can be seen from the figure that β
376 $= 0.35 \pm 0.05 \text{ km}^{-1}$ and $H' = 80 \pm 1 \text{ km}$ would produce the observed changes in the VLF signals
377 when uncertainty limits are taken into account. This solution explains the observed changes over
378 all four paths, although in practice there are a wider range of solutions that could describe the
379 amplitude perturbation levels, and the result is primarily constrained by the phase perturbation
380 levels. We further use this information to show that the shape of the precipitation-perturbed
381 ionospheric profile determined from Van Allen Probes data is consistent with the β/H'
382 modelling profile found with the approach undertaken here, and use it to calculate the equivalent
383 relativistic flux that matches the β/H' modelling profile that might be coming into the
384 atmosphere during the dropout observed on 17 March 2015.

385 **4.2 Energetic Electron Precipitation (EEP) Modelling**

386 From our earlier analysis we know both the electron density profiles which describe (a)
387 the undisturbed ionospheric D-region, and (b) changes incurred by EEP during the dropout
388 event. We also know parameters to describe the nature of electron flux lost from the outer
389 radiation belt, potentially entering the ionosphere, i.e., the energy range and pitch angle
390 distribution. Our goal is to determine the magnitude of the EEP flux, such that we can estimate
391 the importance of EEP to the observed dropout at $L \sim 4$. We follow the same processes described
392 in earlier studies to determine the EEP affected electron density profiles (following, for
393 example Rodger et al. (2013) and Simon-Wedlund et al. (2014)). The EEP produced ionization

394 rate is calculated for a range of EEP fluxes, assuming a power law energy spectrum with
395 gradient -8.8 found in section 3.1. We assume the EEP spans the energy range of 900-6300keV,
396 based on the Van Allen Probes observations of which energy channels showed decreased flux
397 levels during the dropout event, with the range bounded by the energy channels that did not
398 show any flux decreases. From these ionization rates the disturbed ionospheric electron density
399 profile is determined, and the flux is identified which most closely produce the mid-range
400 $\beta=0.35$, $H'=80$ km profile determined in section 4.1.

401 The result of these calculations are shown in Figure 8. The undisturbed electron density
402 profile is shown by the black line, representing a pre-event Wait ionosphere ($\beta=0.63$,
403 $H'=85.1$ km) up to 90 km altitude, which then smoothly transitions to a profile provided by the
404 International Reference Ionosphere (IRI-2007) appropriate for the middle of the propagation
405 paths (50° N, 270° E). The heavy dashed blue line in Figure 8 is the disturbed Wait ionosphere
406 ($\beta=0.35$, $H'=80$ km), while the lighter blue, green, red lines are the best fitting electron density
407 profiles produced by the EEP modelling. We investigated the sensitivity of the EEP produced
408 electron number density profile to the choice of the ambient nighttime profile. In practice the
409 magnitude of the EEP produced ionization is so dominant that it produces the same EEP
410 ionization profile for a very wide range of ambient profiles, and thus although the VLF phase
411 and amplitude analysis provides a clear indication of the nighttime ambient profile
412 characteristics, it does not influence the final EEP ionization profile result significantly. Note
413 that there is a fairly good agreement between the shape of the number density profiles produced
414 by the EEP and the Wait ionosphere over the altitude range 55-90 km, inside which the VLF
415 reflections will take place. Although the two profiles can be seen to diverge below number
416 density levels of 10^{-1} el.cm⁻³, and the gradient becomes markedly steeper than ambient, the

417 subionospheric VLF radiowaves are insensitive to these densities, and independent of the
418 electron number density profile characteristics at these altitudes (<55km) at night. While the
419 EEP has an energy range starting at 900 keV, for the purpose of comparison with the dropout,
420 we label these through their 2 MeV flux values. Those are 2.1×10^{-3} el.cm⁻²s⁻¹keV⁻¹, 2.7×10^{-3}
421 3 el.cm⁻²s⁻¹keV⁻¹, and 3.4×10^{-3} el.cm⁻²s⁻¹keV⁻¹, respectively.

422 **5. Flux tube total content changes**

423 Our goal is to determine how significant these EEP fluxes are to the observed electron
424 flux dropout, i.e., how much of the dropout is due to precipitation into the atmosphere. To do
425 this we calculate the total population of electrons in a flux tube at a given energy, and
426 determine the time required to deplete this tube to the RBSP observed levels. This is a fairly
427 common approach used in experimental studies to determine the overall significance of
428 precipitation to the radiation belts (e.g., Voss et al., 1998; Lorentzen et al., 2001; Rodger et al.,
429 2003; O'Brien et al., 2004; Blum et al., 2013).

430 As noted above, the D-region electron density profile consistent with the VLF
431 observations can be produced by EEP with a relatively small range of flux magnitudes. For the
432 purposes of the following comparison we take the middle value. Note that this choice has no
433 significant impact on the conclusions. At 0724 UT, near the beginning of the dropout, RBSP-A
434 passed through L=4 and determined the trapped 2 MeV flux and pitch angle distribution, as
435 described above. We use this information to determine the number of 2 MeV electrons in a
436 magnetic flux tube of 1 square centimeter in area at the equatorial plane, and then transform
437 this value to the top of atmosphere at 100 km (in both cases following the methodology
438 described by Voss et al. (1998) and Rodger et al. (2003)). This leads to a flux tube total 2 MeV
439 electron population of 1.2×10^4 electrons. In contrast, at 1318 UT, near the end of the dropout,

440 the RBSP observations indicate the flux tube total 2 MeV electron population was 695
441 electrons. From this we see that there was a ~95% decrease in the total flux tube content at this
442 energy. However, the EEP at 2 MeV that we have calculated above would take slightly more
443 than 50 days to cause such a large decrease. As the ~95% decrease occurred in ~7 hours, it is
444 clear that very little of the dropout can be explained through precipitation into the atmosphere.
445 At the specific EEP rate we would expect the total tube content to only decrease by <0.5%, by
446 considering the 900-6300 keV electron flux.

447 We have also undertaken the same calculation for 3.6 MeV, where the dropout was
448 >98%. For the VLF determined EEP rate, it would take 45 days to drain the flux tube content to
449 this level, again, vastly longer than experimentally observed. If some of the VLF phase and
450 amplitude perturbations are due to the precipitation of electrons with lower electron energy (i.e.,
451 <900 keV), then the flux of 900-6300 keV electrons that we calculate here would consequently
452 be even smaller than stated. Therefore, in this study the maximum loss of 900-6300 keV
453 electrons that could have occurred during the dropout event is determined, and it could
454 potentially be smaller than this. We note that precipitation at lower energies than the relativistic
455 ones assumed here could have influenced the size of the radio wave perturbations. Thus, the flux
456 of relativistic electrons that have been determined in this study could have been even smaller
457 than those calculated as a result of our working assumption (i.e., that all of the perturbation was
458 due to relativistic flux). There is even the possibility that the entire VLF perturbation observed
459 could have been generated by lower energy precipitation (100's of keV or so) such that there was
460 no relativistic precipitation involved in the observed perturbations. However, this is unlikely due
461 to the fact that some relativistic electron precipitation was observed by the POES satellites at the
462 beginning of the dropout period. Thus, this study calculates an upper limit of the likely

463 relativistic fluxes involved. From this we conclude that EEP played only a very small role in the
464 observed electron flux dropout.

465 **6. Discussion and Summary**

466 Many previous studies have focused on the loss mechanism of outer belt electron flux
467 (Dessler and Karplus, 1960; West et al., 1973; Imhof and Gaines et al., 1993; Thorne et al., 2005;
468 Ukhorsky et al., 2006; Baker et al., 2016) but very few of them gave attention to relative
469 contribution of each physical mechanism (Li et al., 1997; Onsager et al., 2002; Bortnik et al.,
470 2006; Morley et al., 2010; Yu et al., 2013; Xiang et al., 2017). In this paper, we have determined
471 the fraction of the outer-belt relativistic electrons at $L \sim 4$ that could have precipitated into the
472 atmosphere during the dropout event that occurred during the St. Patrick's Day storm of 2015.
473 We assume that the perturbations observed on ground-based narrow-band VLF radio waves are
474 entirely due to relativistic electron precipitation associated with the dropout observed by the Van
475 Allen probes, and thus calculate an upper limit of the likely relativistic fluxes involved. A
476 dropout of electrons with energies in the range from 900 keV to 6.3 MeV was seen through
477 RBSP's flux measurements starting at ~ 0630 UT on 17 March 2015 over $L=3.5-6$ with a power
478 law energy spectral gradient of -8.8 at 15° pitch angle, i.e., close to the atmospheric loss cone.
479 Strong perturbations in VLF narrowband transmitter signals for four $L \approx 3$ to 4.5 paths, i.e.,
480 NAA-Seattle, NAA-Edmonton, NML-St. John's and NML-Edmonton, are observed for nearly
481 two hours starting at the same time as the dropout. Phase increases of $\sim 180^\circ$ are typically
482 observed on the four paths analysed from ~ 0630 to 0830 UT. LWPC modelling is performed to
483 infer the ionospheric changes that occurred at the time of the dropout, using Wait ionospheric
484 parameterization. We found that $\beta = 0.35 \text{ km}^{-1}$ and $H' = 80 \text{ km}$ would produce the observed
485 changes in VLF signal. The power law gradient and pitch angle distributions from RBSP, as well

486 as Wait ionospheric parameters from VLF radio wave observations, are used to calculate total
487 tube content, and subsequent EEP loss rates. The results suggest that it would take 50 days to
488 drain a flux tube of 2 MeV electrons and 45 days to drain the 3.6 MeV flux at $L \approx 4$. However, the
489 satellite observations suggest that the flux decrease to drain the flux tube by 95% only took ~ 7
490 hours. Our calculations indicate that during this time interval only $<0.5\%$ of the relativistic fluxes
491 (900-6300 keV) could have been lost to the atmosphere. This leads to the conclusion that a very
492 minimal fraction of the total trapped relativistic flux entered the atmosphere as a result of the
493 dropout at $L=3$ to 4.5, and electron precipitation was not the major contributor to the observed
494 dropout during the St. Patrick's Day storm of 2015.

495 **Acknowledgements**

496 SAG benefited from the SCOSTEP Visiting Scholar Program, under which she visited South
497 African National Space Agency (SANSA), South Africa, where this research was initiated. SAG
498 would like to thank Tongji University for the post-doctoral fund. SAG also thanks Claudia
499 Martinez (ISEE, Nagoya University) for her timely technical help. Authors from Indian Institute
500 of Geomagnetism (IIG) are grateful to Director, IIG, for support and encouragement to carry out
501 the work. We thank ACE, Wind and OMNIWeb (<https://omniweb.gsfc.nasa.gov/form/dx1.html>)
502 teams for providing solar wind data. We acknowledge the RBSP data providers J. Bernard Blake
503 (The Aerospace Corporation), D. Baker (University of Colorado at Boulder). This data can be
504 found on CDAWeb (<https://cdaweb.sci.gsfc.nasa.gov/>). The subionospheric VLF data can be
505 found at the Polar Data Centre
506 (<http://psddb.nercbas.ac.uk/data/access/main.php?menu=1,7&source=1&script=1>). The authors
507 would also like to acknowledge useful discussions with Alyson Jaynes regarding the RBSP data
508 analysis. MAC would like to acknowledge support from the Natural Environment Research

509 Council (UKRI-NERC) Highlight Topic grant NE/P01738X/1 (Rad-Sat), and support from the
510 Royal Society Newton Fund International exchanges award 2015.

511 **References**

512 Anderson, B. J., and Hamilton, D. C. (1993). Electromagnetic ion cyclotron waves stimulated by
513 modest magnetospheric compressions. *Journal of Geophysical Research: Space Physics*, 98(A7),
514 11369-11382, <https://doi.org/10.1029/93JA00605>

515 Baker, D. N., Jaynes, A. N., Kanekal, S. G., Foster, J. C., Erickson, P. J., Fennell, J. F., &
516 Henderson, M. G. (2016). Highly relativistic radiation belt electron acceleration, transport, and
517 loss: Large solar storm events of March and June 2015. *Journal of Geophysical Research: Space*
518 *Physics*, 121(7), 6647-6660, <https://doi.org/10.1002/2016JA022502>

519 Behera, J. K., Sinha, A. K., Vichare, G., Bhaskar, A., Honary, F., Rawat, R., & Singh, R. (2017).
520 Enhancement and modulation of cosmic noise absorption in the afternoon sector at subauroral
521 location (L= 5) during the recovery phase of 17 March 2015 geomagnetic storm. *Journal of*
522 *Geophysical Research: Space Physics*, 122(9), 9528-9544,
523 <https://doi.org/10.1002/2017JA024226>

524 Blum, L. W., Schiller, Q., Li, X., Millan, R., Halford, A., & Woodger, L. (2013). New
525 conjunctive CubeSat and balloon measurements to quantify rapid energetic electron
526 precipitation, *Geophys. Res. Lett.*, 40, 5833–5837, doi:10.1002/2013GL058546

527 Bortnik, J., Thorne, R. M., O'Brien, T. P., Green, J. C., Strangeway, R. J., Shprits, Y. Y., &
528 Baker, D. N. (2006). Observation of two distinct, rapid loss mechanisms during the 20

529 November 2003 radiation belt dropout event. *Journal of Geophysical Research: Space Physics*,
530 111(A12), doi:10.1029/2006JA011802

531 Boyd, A. J., Spence, H. E., Claudepierre, S. G., Fennell, J. F., Blake, J. B., Baker, D. N., ... &
532 Turner, D. L. (2014). Quantifying the radiation belt seed population in the 17 March 2013
533 electron acceleration event. *Geophysical Research Letters*, 41(7), 2275-2281,
534 <https://doi.org/10.1002/2014GL059626>

535 Boynton, R. J., Mourenas, D., & Balikhin, M. A. (2016). Electron flux dropouts at Geostationary
536 Earth Orbit: Occurrences, magnitudes, and main driving factors. *Journal of Geophysical*
537 *Research: Space Physics*, 121(9), 8448-8461, <https://doi.org/10.1002/2016JA022916>

538 Clilverd, M. A., Duthie, R., Hardman, R., Hendry, A. T., Rodger, C. J., Raita, T., & Milling, D.
539 K. (2015). Electron precipitation from EMIC waves: A case study from 31 May 2013. *Journal of*
540 *Geophysical Research: Space Physics*, 120(5), 3618-3631,
541 <https://doi.org/10.1002/2015JA021090>

542 Clilverd, M. A., Rodger, C. J., Brundell, J. B., Cobbett, N., Bähr, J., Moffat-Griffin, T.,
543 Kavanagh, A. J., Seppälä, A., Thomson, N. R., Friedel, R. H. W., & Menk, F. W. (2008).
544 Energetic electron precipitation during sub-storm injection events: high latitude fluxes and an
545 unexpected mid-latitude signature. *J. Geophys. Res.*, 113, A10311, doi: 10.1029/2008JA013220

546 Clilverd, M. A., Rodger, C. J., Danskin, D., Usanova, M. E., Raita, T., Ulich, Th., & Spanswick,
547 E. L. (2012). Energetic Particle injection, acceleration, and loss during the geomagnetic
548 disturbances which upset Galaxy 15. *J. Geophys. Res.*, 117, A12213,
549 doi:10.1029/2012JA018175

550 Clilverd, M. A., Rodger, C. J., Thomson, N. R., Brundell, J. B., Ulich, T., Lichtenberger, J., ... &
551 Verronen, P. T. (2009). Remote sensing space weather events: Antarctic-Arctic radiation-belt
552 (dynamic) deposition-VLF Atmospheric Research Konsortium network. *Space Weather*, 7(4), 1-
553 15, <https://doi.org/10.1029/2008SW000412>

554 Cornwall, J. M. (1965). Cyclotron instabilities and electromagnetic emission in the ultra low
555 frequency and very low frequency ranges. *Journal of Geophysical Research*, 70(1), 61-69,
556 <https://doi.org/10.1029/JZ070i001p00061>

557 Dessler, A. J., and Karplus, R. (1960). Some properties of the Van Allen radiation. *Physical*
558 *Review Letters*, 4(6), 271, doi: 10.1103/PhysRevLett.4.271

559 Erlandson, R. E., and Ukhorskiy, A. J. (2001). Observations of electromagnetic ion cyclotron
560 waves during geomagnetic storms: Wave occurrence and pitch angle scattering. *Journal of*
561 *Geophysical Research: Space Physics*, 106(A3), 3883-3895,
562 <https://doi.org/10.1029/2000JA000083>

563 Ferguson, J. A. (1998). Computer Programs for Assessment of Long-Wavelength Radio
564 Communications, Version 2.0: User's Guide and Source Files (No. TD-3030). Space and naval
565 warfare systems center san diego ca.

566 Fraser, B. J., Singer, H. J., Hughes, W. J., Wygant, J. R., Anderson, R. R., & Hu, Y. D. (1996).
567 CRRES Poynting vector observations of electromagnetic ion cyclotron waves near the
568 plasmopause. *Journal of Geophysical Research: Space Physics*, 101(A7), 15331-15343,
569 doi:10.1029/95JA03480

570 Glauert, S. A., Horne, R. B., & Meredith, N. P. (2018). A 30-year simulation of the outer
571 electron radiationbelt. *Space Weather*, 16, 1498–1522, <https://doi.org/10.1029/2018SW001981>

572 Green, J. C., Onsager, T. G., O'Brien, T. P., & Baker, D. N. (2004). Testing loss mechanisms
573 capable of rapidly depleting relativistic electron flux in the Earth's outer radiation belt. *Journal of*
574 *Geophysical Research: Space Physics*, 109(A12), doi:10.1029/2004JA010579

575 Hardman, R., Clilverd, M. A., Rodger, C. J., Brundell, J. B., Duthie, R., Holzworth, R. H., Mann,
576 I. R., Milling, D. K., & Macusova. E. (2015). A case study of electron precipitation fluxes due to
577 plasmaspheric hiss. *J. Geophys. Res. Space Physics*, 120, 6736–6748,
578 doi:10.1002/2015JA021429

579 Hendry, A. T., Rodger, C. J., & Clilverd, M. A. (2017). Evidence of sub - MeV EMIC - driven
580 electron precipitation. *Geophysical Research Letters*, 44(3), 1210-1218,
581 <https://doi.org/10.1002/2016GL071807>

582 Hendry, A. T., Rodger, C. J., Clilverd, M. A., Thomson, N. R., Morley, S. K., & Raita, T.
583 (2012). Rapid radiation belt losses occurring during high speed solar wind stream driven storms:
584 Importance of energetic electron precipitation. *Dynamics of the Earth's Radiation Belts and*
585 *Inner Magnetosphere*, 199, 213-223, <https://doi.org/10.1029/2012GM001299>

586 Herrera, D., Maget, V. F., & Sicard - Piet, A. (2016). Characterizing magnetopause shadowing
587 effects in the outer electron radiation belt during geomagnetic storms. *Journal of Geophysical*
588 *Research: Space Physics*, 121(10), 9517-9530, doi:10.1002/2016JA022825

589 Horne, R. B., and Thorne, R. M. (1998). Potential waves for relativistic electron scattering and
590 stochastic acceleration during magnetic storms. *Geophysical Research Letters*, 25(15), 3011-
591 3014, <https://doi.org/10.1029/98GL01002>

592 Horne, R. B., Thorne, R. M., Glauert, S. A., Albert, J. M., Meredith, N. P., & Anderson, R. R.
593 (2005). Timescale for radiation belt electron acceleration by whistler mode chorus waves.
594 *Journal of Geophysical Research: Space Physics*, 110(A3), doi:10.1029/2004JA010811.

595 Imhof, W. L., & Gaines, E. E. (1993). Inputs to the atmosphere from relativistic electrons.
596 *Journal of Geophysical Research: Space Physics*, 98(A8), 13575-13580,
597 <https://doi.org/10.1029/93JA01149>

598 Kennel, C. F., & Petschek, H. E. (1966). Limit on stably trapped particle fluxes. *Journal of*
599 *Geophysical Research*, 71(1), 1-28, <https://doi.org/10.1029/JZ071i001p00001>

600 Kim, H. J., & Chan, A. A. (1997). Fully adiabatic changes in storm time relativistic electron
601 fluxes. *Journal of Geophysical Research: Space Physics*, 102(A10), 22107-22116,
602 doi:10.1029/97JA01814

603 Kim, K. C., Lee, D. Y., Kim, H. J., Lyons, L. R., Lee, E. S., Öztürk, M. K., & Choi, C. R.
604 (2008). Numerical calculations of relativistic electron drift loss effect. *Journal of Geophysical*
605 *Research: Space Physics*, 113(A9), doi:10.1029/2007JA013011

606 Kivelson, M. G., and Russell, C. T. (Eds.). (1995). Introduction to space physics. Cambridge
607 university press.

608 Kozyra, J. U., Cravens, T. E., Nagy, A. F., Fontheim, E. G., & Ong, R. S. B. (1984). Effects of
609 energetic heavy ions on electromagnetic ion cyclotron wave generation in the plasmopause
610 region. *Journal of Geophysical Research: Space Physics*, 89(A4), 2217-2233,
611 <https://doi.org/10.1029/JA089iA04p02217>

612 Li, X., Baker, D.N., Temerin, M., Caytone, T.E., Reeves, E.G.D., Christensen, R.A., Blake, J.B.,
613 Looper, M.D., Nakamura, R., & Kanekal, S.G. (1997). Multisatellite observations of the outer
614 zone electron variation during the November 3–4, 1993 magnetic storm. *Journal of Geophysical*
615 *Research* 102, 14123–14140, <https://doi.org/10.1029/97JA01101>

616 Li, W., Shprits, Y. Y., and Thorne, R. M. (2007). Dynamic evolution of energetic outer zone
617 electrons due to wave - particle interactions during storms. *Journal of Geophysical Research:*
618 *Space Physics*, 112(A10), doi:10.1029/2007JA012368

619 Li, W., Thorne, R. M., Angelopoulos, V., Bortnik, J., Cully, C. M., Ni, B., and Magnes, W.
620 (2009). Global distribution of whistler - mode chorus waves observed on the THEMIS
621 spacecraft. *Geophysical Research Letters*, 36(9), doi:10.1029/2009GL037595

622 Lorentzen, K. R., M. D. Looper, and J. B. Blake (2001), Relativistic electron microbursts during
623 the GEM storms, *Geophys. Res. Lett.*, 28, 2573–2576, doi:10.1029/2001GL012926

624 Loto'Aniu, T. M., Fraser, B. J., and Waters, C. L. (2005). Propagation of electromagnetic ion
625 cyclotron wave energy in the magnetosphere. *Journal of Geophysical Research: Space Physics*,
626 110(A7), doi:10.1029/2004JA010816

627 Lyons, L. R., and Thorne, R. M. (1973). Equilibrium structure of radiation belt electrons.
628 *Journal of Geophysical Research*, 78(13), 2142-2149, <https://doi.org/10.1029/JA078i013p02142>

629 Mauk, B. H., Fox, N. J., Kanekal, S. G., Kessel, R. L., Sibeck, D. G., and Ukhorskiy, A. (2012).
630 Science objectives and rationale for the Radiation Belt Storm Probes mission. In *The Van Allen*
631 *Probes Mission* (pp. 3-27). Springer, Boston, MA., <https://doi.org/10.1007/s11214-012-9908-y>

632 McIlwain, C. E. (1966). Ring current effects on trapped particles. *Journal of Geophysical*
633 *Research*, 71(15), 3623-3628, [://doi.org/10.1029/JZ071i015p03623](https://doi.org/10.1029/JZ071i015p03623)

634 Meredith, N. P., Horne, R. B., and Anderson, R. R. (2001). Substorm dependence of chorus
635 amplitudes: Implications for the acceleration of electrons to relativistic energies. *Journal of*
636 *Geophysical Research: Space Physics*, 106(A7), 13165-13178,
637 <https://doi.org/10.1029/2000JA900156>

638 Meredith, N. P., Thorne, R. M., Horne, R. B., Summers, D., Fraser, B. J., and Anderson, R. R.
639 (2003). Statistical analysis of relativistic electron energies for cyclotron resonance with EMIC
640 waves observed on CRRES. *Journal of Geophysical Research: Space Physics*, 108(A6),
641 [doi:10.1029/2002JA009700](https://doi.org/10.1029/2002JA009700)

642 Millan, R. M., and Thorne, R. M. (2007). Review of radiation belt relativistic electron losses.
643 *Journal of Atmospheric and Solar-Terrestrial Physics*, 69(3), 362-377,
644 <https://doi.org/10.1016/j.jastp.2006.06.019>

645 Miyoshi, Y., Morioka, A., Misawa, H., Obara, T., Nagai, T., and Kasahara, Y. (2003).
646 Rebuilding process of the outer radiation belt during the 3 November 1993 magnetic storm:
647 NOAA and Exos - D observations. *Journal of Geophysical Research: Space Physics*, 108(A1),
648 SMP-3, [doi:10.1029/2001JA007542](https://doi.org/10.1029/2001JA007542)

649 Miyoshi, Y., Sakaguchi, K., Shiokawa, K., Evans, D., Albert, J., Connors, M., and Jordanova, V.
650 (2008). Precipitation of radiation belt electrons by EMIC waves, observed from ground and
651 space. *Geophysical Research Letters*, 35(23), doi:10.1029/2008GL035727

652 Morfitt, D. G., and Shellman, C. H. (1976). 'MODESRCH', An Improved Computer Program for
653 Obtaining ELF/VLF/LF Mode Constants in an Earth-Ionosphere Waveguide (No. NELC/IR-
654 77T). Naval Electronics Lab Center San Diego CA

655 Morley, S. K., R. H. W. Friedel, E. L. Spanswick, G. D. Reeves, J. T. Steinberg, J. Koller, T.
656 Cayton, and E. Noveroske (2010), Dropouts of the outer electron radiation belt in response to
657 solar wind stream interfaces: global positioning system observations. *Proc. R. Soc. A*, 466, 3329-
658 3350, doi:10.1098/rspa.2010.0078

659 Ni, B., Liang, J., Thorne, R. M., Angelopoulos, V., Horne, R. B., Kubyshkina, M., ... and
660 Lummerzheim, D. (2012). Efficient diffuse auroral electron scattering by electrostatic electron
661 cyclotron harmonic waves in the outer magnetosphere: A detailed case study. *Journal of*
662 *Geophysical Research: Space Physics*, 117(A1), doi:10.1029/2011JA017095

663 O'Brien, T. P., M. D. Looper, and J. B. Blake (2004), Quantification of relativistic electron
664 microburst losses during the GEM storms, *Geophys. Res. Lett.*, 31, L04802,
665 doi:10.1029/2003GL018621

666 Onsager, T. G., G. Rostoker, H.-J. Kim, G. D. Reeves, T. Obara, H. J. Singer, and C. Smithtro,
667 (2002). Radiation belt electron flux dropouts: Local time, radial, and particle-energy dependence,
668 *J. Geophys. Res.*, 107(A11), 1382, doi:10.1029/2001JA000187

669 Reeves, G. D., McAdams, K. L., Friedel, R. H. W., and O'Brien, T. P. (2003). Acceleration and
670 loss of relativistic electrons during geomagnetic storms. *Geophysical Research Letters*, 30(10),
671 doi:10.1029/2002GL016513

672 Reeves, G. D., Spence, H. E., Henderson, M. G., Morley, S. K., Friedel, R. H. W., Funsten, H.
673 O., and Claudepierre, S. G. (2013). Electron acceleration in the heart of the Van Allen radiation
674 belts. *Science*, 341(6149), 991-994, doi:10.1126/science.1237743

675 Rodger, C. J., A. J. Kavanagh, M. A. Clilverd, and S. R. Marple (2013), Comparison between
676 POES energetic electron precipitation observations and riometer absorptions: Implications for
677 determining true precipitation fluxes, *J. Geophys. Res. Space Physics*, 118, 7810–7821,
678 doi:10.1002/2013JA019439

679 Rodger, C. J., Clilverd, M.A., Green, J., and Lam, M-M. (2010). Use of POES SEM-2
680 observations to examine radiation belt dynamics and energetic electron precipitation in to the
681 atmosphere., *Journal of Geophysical Research: Space Physics*, 115, A04202, doi:10.1029/
682 2008JA014023

683 Rodger, C. J., Clilverd, M. A., and McCormick, R. J. (2003). Significance of lightning-generated
684 whistlers to inner radiation belt electron lifetimes. *J. Geophys. Res.*, 108(A12), 1462,
685 doi:10.1029/2003JA009906

686 Rodger, C. J., Raita, T., Clilverd, M. A., Seppälä, A., Dietrich, S., Thomson, N. R., and Ulich, T.
687 (2008). Observations of relativistic electron precipitation from the radiation belts driven by
688 EMIC waves. *Geophysical Research Letters*, 35(16), doi:10.1029/2008GL034804

689 Rodger, C. J., Clilverd, M. A., Kavanagh, A. J., Watt, C. E., Verronen, P. T., & Raita, T. (2012).
690 Contrasting the responses of three different ground - based instruments to energetic electron
691 precipitation. *Radio Science*, 47(2), doi:10.1029/2011RS004971

692 Sazhin, S. S., and Hayakawa, M. (1992). Magnetospheric chorus emissions: A review. *Planetary*
693 *and space science*, 40(5), 681-697, [https://doi.org/10.1016/0032-0633\(92\)90009-D](https://doi.org/10.1016/0032-0633(92)90009-D)

694 Schulz, M., and Lanzerotti, L. J. (1974). Particle diffusion in the radiation belts (Vol. 7).
695 *Springer Science and Business Media*, Springer, Berlin, Heidelberg,
696 <https://doi.org/10.1007/978-3-642-65675-0>

697 Shprits, Y. Y., Kellerman, A., Aseev, N., Drozdov, A. Y., and Michaelis, I. (2017). Multi - MeV
698 electron loss in the heart of the radiation belts. *Geophysical Research Letters*, 44(3), 1204-1209,
699 <https://doi.org/10.1002/2016GL072258>

700 Simon Wedlund, M., M. A. Clilverd, C. J. Rodger, K. Cresswell-Moorcock, N. Cobbett, P.
701 Breen, D. Danskin, E. Spanswick, and J. V. Rodriguez (2014), A statistical approach to
702 determining energetic outer radiation belt electron precipitation fluxes, *J. Geophys. Res. Space*
703 *Physics*, 119, 3961–3978, doi:10.1002/2013JA019715

704 Summers, D., and Thorne, R. M. (2003). Relativistic electron pitch - angle scattering by
705 electromagnetic ion cyclotron waves during geomagnetic storms. *J. Geophys. Res. Space*
706 *Physics*, 108(A4), doi:10.1029/2002JA009489

707 Summers, D., Thorne, R. M., and Xiao, F. (1998). Relativistic theory of wave - particle resonant
708 diffusion with application to electron acceleration in the magnetosphere. *J. Geophys. Res. Space*
709 *Physics*, 103(A9), 20487-20500.

710 Temerin, M., Roth, I., Hudson, M. K., and Wygant, J. R. (1994). New paradigm for the transport
711 and energization of radiation belt particles. *Eos Trans. AGU*, 75(44), 538

712 Thomson, N. R., Clilverd, M. A., and McRae, W. M. (2007). Nighttime ionospheric D region
713 parameters from VLF phase and amplitude. *J. Geophys. Res. Space Physics*, 112(A7),
714 doi:10.1029/2007JA012271

715 Thomson, N. R., Rodger, C. J., & Clilverd, M. A. (2005). Large solar flares and the ionospheric
716 D-region enhancements. *J. Geophys. Res. Space Physics.*, 110, A06306,
717 doi:10.1029/2005JA011008

718 Thomson, N. R., Clilverd, M. A., & Rodger, C. J. (2011a). Daytime midlatitude D region
719 parameters at solar minimum from short - path VLF phase and amplitude. *J. Geophys. Res.*
720 *Space Physics*, 116(A3), doi:10.1029/2010JA016248

721 Thomson, N. R., and McRae, W. M. (2009). Nighttime ionospheric D region: Equatorial and
722 Non-equatorial. *J. Geophys. Res. Space Physics*, 114, A08305, doi:10.1029/2008JA014001

723 Thomson, N. R., Rodger, C. J., & Clilverd, M. A. (2011b). Daytime D region parameters from
724 long - path VLF phase and amplitude. *J. Geophys. Res. Space Physics*, 116(A11),
725 doi:10.1029/2011JA016910

726 Thorne, R. M., and Kennel, C. F. (1971). Relativistic electron precipitation during magnetic
727 storm main phase. *Journal of Geophysical research*, 76(19), 4446-4453,
728 <https://doi.org/10.1029/JA076i019p04446>

729 Thorne, R. M., Church, S. R., and Gorney, D. J. (1979). On the origin of plasmaspheric hiss: The
730 importance of wave propagation and the plasmopause. *Journal of Geophysical Research: Space*
731 *Physics*, 84(A9), 5241-5247, <https://doi.org/10.1029/JA084iA09p05241>

732 Thorne, R. M., Li, W., Ni, B., Ma, Q., Bortnik, J., Chen, L., and Kletzing, C. A. (2013). Rapid
733 local acceleration of relativistic radiation-belt electrons by magnetospheric chorus. *Nature*,
734 504(7480), 411, <https://doi.org/10.1038/nature12889>

735 Thorne, R. M., O'Brien, T. P., Shprits, Y. Y., Summers, D., and Horne, R. B. (2005). Timescale
736 for MeV electron microburst loss during geomagnetic storms. *Journal of Geophysical Research:*
737 *Space Physics*, 110(A9), doi:10.1029/2004JA010882

738 Thorne, R. M., Smith, E. J., Burton, R. K., and Holzer, R. E. (1973). Plasmaspheric hiss. *Journal*
739 *of Geophysical Research*, 78(10), 1581-1596, <https://doi.org/10.1029/JA078i010p01581>

740 Tsurutani, B. T., and Smith, E. J. (1974). Postmidnight chorus: A substorm phenomenon.
741 *Journal of Geophysical Research*, 79(1), 118-127, <https://doi.org/10.1029/JA079i001p00118>

742 Tsurutani, B. T., Hajra, R., Tanimori, T., Takada, A., Remya, B., Mannucci, A. J., and Echer, E.
743 (2016). Heliospheric plasma sheet (HPS) impingement onto the magnetosphere as a cause of
744 relativistic electron dropouts (REDs) via coherent EMIC wave scattering with possible
745 consequences for climate change mechanisms. *Journal of Geophysical Research: Space Physics*,
746 121(10), 10.1002/2016JA022499

747 Turner, D. L., Angelopoulos, V., Li, W., Bortnik, J., Ni, B., Ma, Q., ... and Usanova, M. (2014).
748 Competing source and loss mechanisms due to wave - particle interactions in Earth's outer
749 radiation belt during the 30 September to 3 October 2012 geomagnetic storm. *Journal of*
750 *Geophysical Research: Space Physics*, 119(3), 1960-1979,
751 <https://doi.org/10.1002/2014JA019770>

752 Ukhorskiy, A. Y., Anderson, B. J., Brandt, P. C., and Tsyganenko, N. A. (2006). Storm time
753 evolution of the outer radiation belt: Transport and losses. *Journal of Geophysical Research:*
754 *Space Physics*, 111(A11), doi:10.1029/2006JA011690

755 Ukhorskiy, A. Y., Shprits, Y. Y., Anderson, B. J., Takahashi, K., and Thorne, R. M. (2010).
756 Rapid scattering of radiation belt electrons by storm - time EMIC waves. *Geophysical Research*
757 *Letters*, 37(9), doi:10.1029/2010GL042906

758 Voss, H. D., M. Walt, W. L. Imhof, J. Mobilia, and U. S. Inan (1998), Satellite observations of
759 lightning-induced electron precipitation, *J. Geophys. Res.*, 103(A6), 11725–11744,
760 doi:10.1029/97JA02878

761 Wait, J. R., and Spies, K. P. (1964). Characteristics of the Earth-ionosphere waveguide for VLF
762 radio waves (No. 300). US Dept. of Commerce, National Bureau of Standards: for sale by the
763 Supt. of Doc., US Govt. Print. Off

764 Xiang, Z., Tu, W., Li, X., Ni, B., Morley, S. K., and Baker, D. N. (2017). Understanding the
765 mechanisms of radiation belt dropouts observed by Van Allen Probes. *Journal of Geophysical*
766 *Research: Space Physics*, 122(10), 9858-9879, <https://doi.org/10.1002/2017JA024487>

767 West, H. I., Buck, R. M., and Walton, J. R. (1973). Electron pitch angle distributions throughout
768 the magnetosphere as observed on Ogo 5. *Journal of Geophysical Research*, 78(7), 1064-1081,
769 <https://doi.org/10.1029/JA078i007p01064>

770 Wu, C. C., Liou, K., Lepping, R. P., Hutting, L., Plunkett, S., Howard, R. A., and Socker, D.
771 (2016). The first super geomagnetic storm of solar cycle 24: “The St. Patrick’s day event (17
772 March 2015)”. *Earth, Planets and Space*, 68(1), 151, <https://doi.org/10.1186/s40623-016-0525-y>

773 Yando, K., Millan, R. M., Green, J. C., and Evans, D. S. (2011). A Monte Carlo simulation of
774 the NOAA POES Medium Energy Proton and Electron Detector instrument. *Journal of*
775 *Geophysical Research: Space Physics*, 116(A10), doi:10.1029/2011JA016671

776 Yu., Y., J. Koller, and S. K. Morley (2013). Quantifying the effect of magnetopause shadowing
777 on electron radiation belt dropouts. *Ann. Geophys.*, 31, 1929-1939, doi:10.5194/angeo-31-1929-
778 2013

779 Zhang, K., Li, X., Schiller, Q., Gerhardt, D., Zhao, H., and Millan, R. (2017). Detailed
780 characteristics of radiation belt electrons revealed by CSSWE/REPTile measurements:
781 Geomagnetic activity response and precipitation observation. *Journal of Geophysical Research:*
782 *Space Physics*, 122(8), 8434-8445, <https://doi.org/10.1002/2017JA024309>

783 Zhang, X. J., Li, W., Thorne, R. M., Angelopoulos, V., Ma, Q., Li, J., and Reeves, G. D. (2016).
784 Physical mechanism causing rapid changes in ultrarelativistic electron pitch angle distributions
785 right after a shock arrival: Evaluation of an electron dropout event. *Journal of Geophysical*
786 *Research: Space Physics*, 121(9), 8300-8316, <https://doi.org/10.1002/2016JA022517>

787

788

789

790

791

792

793 **Figure Caption**

794 **Figure 1.** Interplanetary conditions measured during the period of interest in our study. This plot
795 shows Wind observations representing solar wind speed (V_{sw}), density (n), pressure (P_{sw}),
796 temperature (T), IMF B_z , SYM-H, and ASY-H. The vertical black line represents the Sudden
797 Storm Commencement (SSC) which occurred at 04:45 UT.

798 **Figure 2.** Locations of VLF transmitters, NAA and NML and receivers Seattle (SEA), St. John's
799 (STJ) and Edmonton (ED) respectively along with great circle paths and L= 3, 4, 5 contours. The
800 magenta and green dots represent the ionospheric footprints of RBSP-A and RBSP-B at $t_1 = 6:30$
801 UT and $t_2 = 8:30$ UT respectively.

802 **Figure 3.** POES P6 trapped (90-deg) and BLC (0-deg) fluxes during 17 March 2015. The colour
803 bar shows the logarithm of the flux (for electron energy >700 keV), while the vertical dotted lines
804 indicate the start and end times of the dropout event, and the horizontal red lines indicate the L-
805 shell range of the VLF paths shown in Figure 2.

806 **Figure 4.** RBSP electron flux from Relativistic Electron Proton Telescope (REPT) for (a) 2.0
807 MeV, (b) 3.6 MeV and (c) 4.2 MeV flux for whole month of March, 2015; (d) 2.0 MeV, (e) 3.6

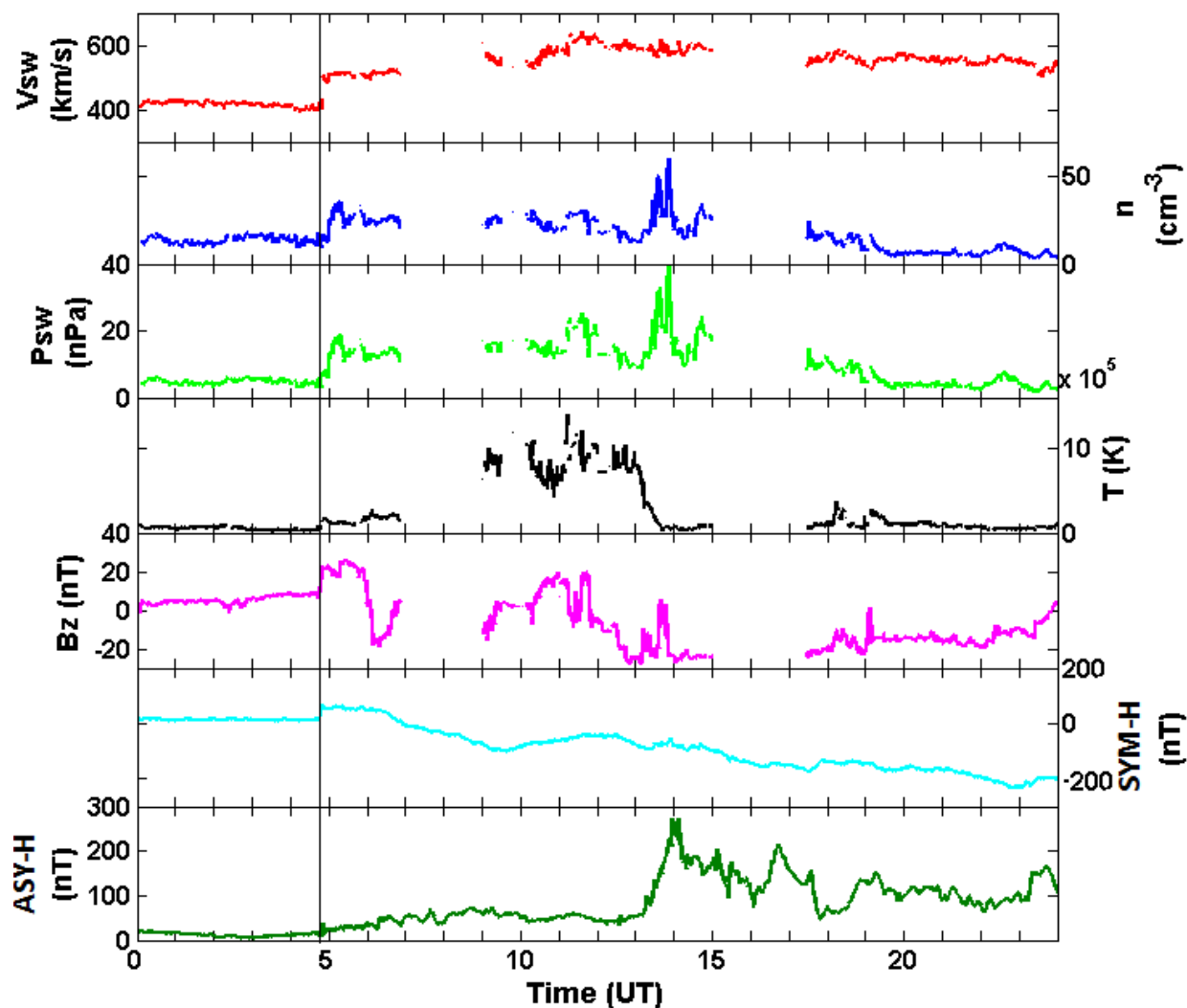
808 MeV and (f) 4.2 MeV flux for 17 and 18 March 2015. RBSP electron flux from MagEIS for (g)
809 226.1 keV, (h) 464.4 keV and (i) 741.6 keV flux for whole month of March, 2015; (j) 226.1 keV,
810 (k) 464.4 keV and (l) 741.6 keV flux for 17 and 18 March 2015. The vertical black lines
811 represent the duration of VLF perturbations analysed in this study.

812 **Figure 5.** (panels a –e) RBSP-A pitch angle distributions for a range of relativistic electron
813 energies at 07:21 UT at L=4 on 17 March 2015. Labels indicate the n parameter fit (using $\sin^n \alpha$)
814 to the observations. Panel f shows the power law energy spectrum at 90° and 15° pitch angles.

815 **Figure 6.** VLF amplitude (left hand column) and phase (right hand column) for the four paths
816 studied (black lines). Panels (a) show the data for 0-24 UT on 17 March 2015. Panels (b) show
817 the 6-9 UT period in more detail. Each individual path is identified on the left hand side of the
818 row. The red curves represent the signal observed on a representative non-disturbed day (marked
819 as the "Quiet Day Curve" (QDC)). Here the blue asterisks show the results of the LWPC
820 modelling to reproduce the undisturbed QDC observations. Vertical black lines represent the
821 duration over which average of the signal is taken. Horizontal green lines in panels (a) represent
822 an estimate of the uncertainty in the pre-event amplitude and phase levels for 3 hours prior to the
823 start time. See text for more details.

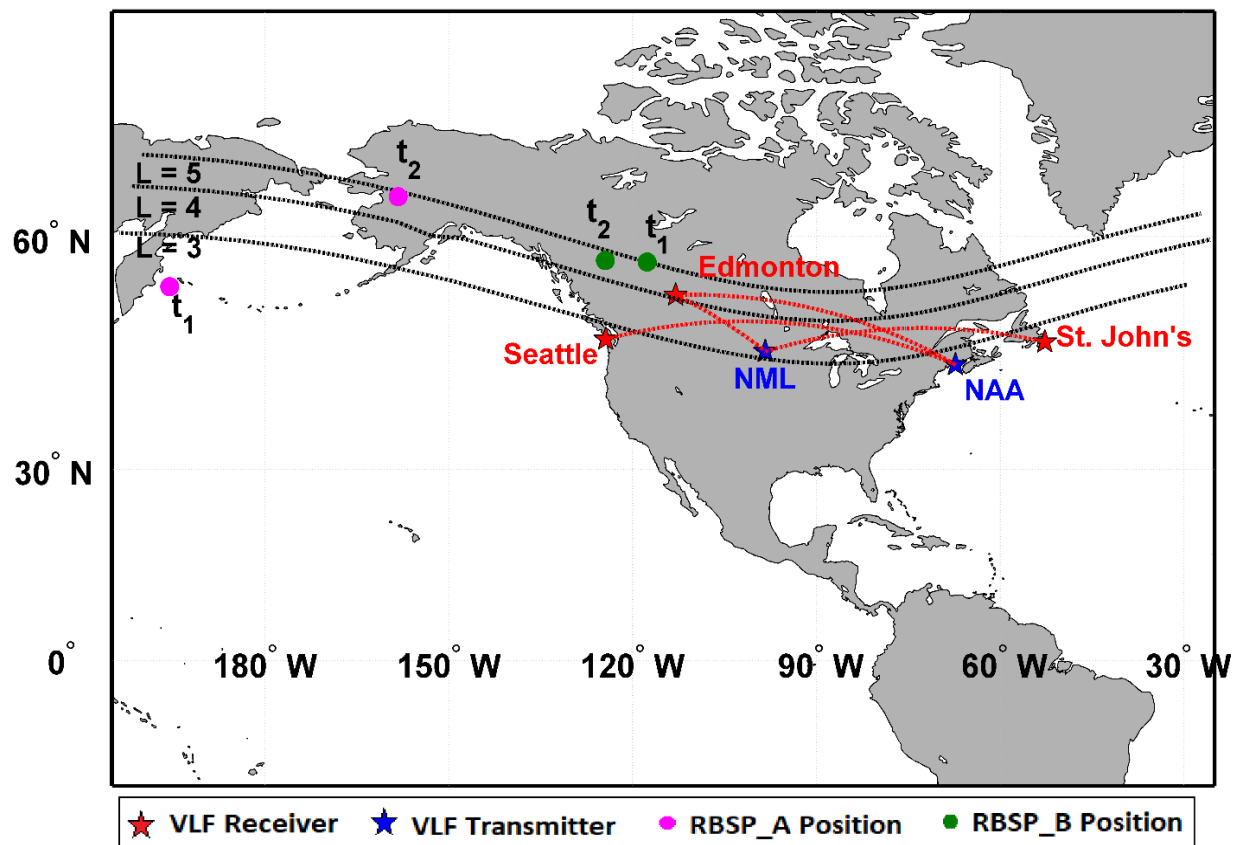
824 **Figure 7.** Variation of the LWPC modelled amplitude and phase of VLF signals as a function of
825 the reference height (H') for varying sharpness factor (β) for the paths: NAA-SEA, NAA-EDM,
826 NML-STJ, and NML-EDM. Observed perturbation levels on each path are indicated by
827 horizontal dot-dashed lines, while the inferred H' solution is shown by a vertical line. The green
828 boxes indicate the uncertainty in perturbation level, and thus the H' solution due to uncertainty in
829 the initial QDC levels. See text for more details.

830 **Figure 8.** D-region electron number density profiles during the dropout event of 17 March 2015.
 831 The black line represents the ambient nighttime profile, while the heavy dashed blue line is the
 832 disturbed Wait ionosphere ($\beta=0.35$, $H'=80$ km) inferred from the VLF observations. Lighter blue,
 833 green, red lines are the best fitting electron densities profiles produced by the EEP modelling
 834 determined from Van Allen Probes data.

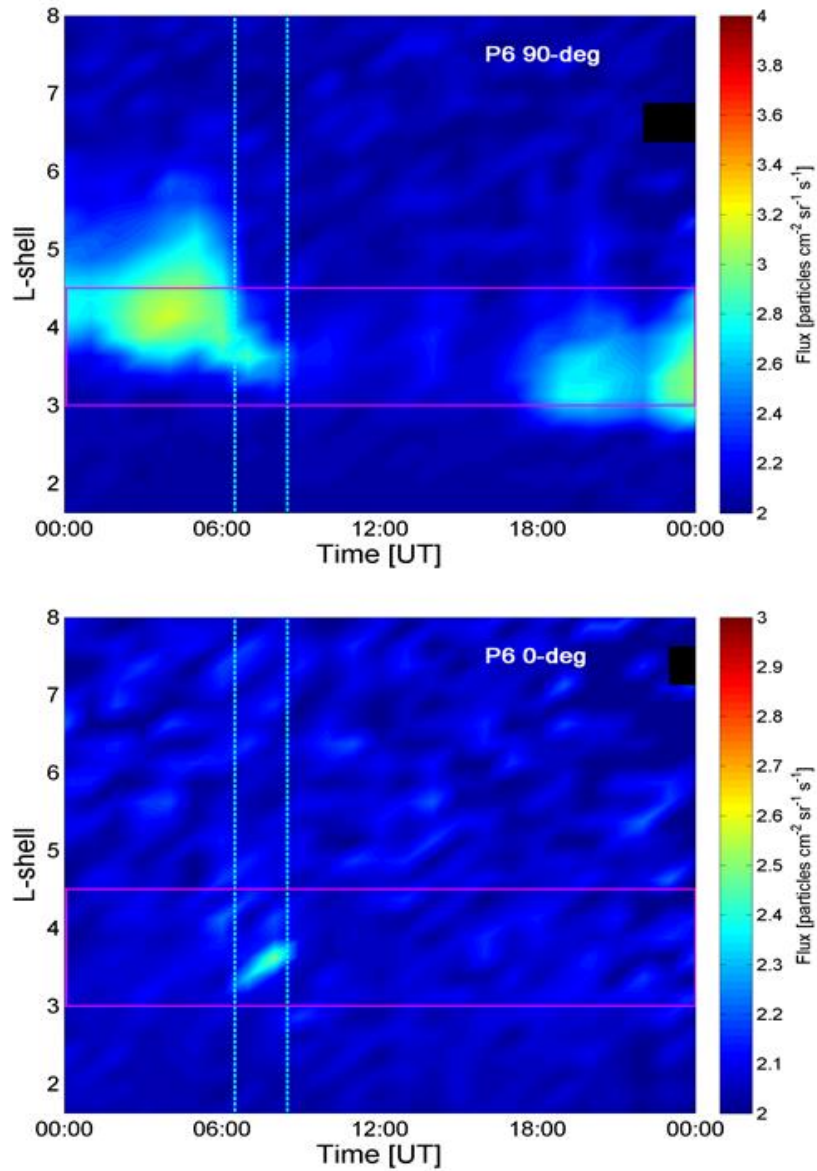


835
 836 **Figure 1.** Interplanetary conditions measured during the period of interest in our study. This plot
 837 shows Wind observations representing solar wind speed (V_{sw}), density (n), pressure (P_{sw}),

838 temperature (T), IMF B_z , SYM-H, and ASY-H. The vertical black line represents the Sudden
839 Storm Commencement (SSC) which occurred at 04:45 UT.

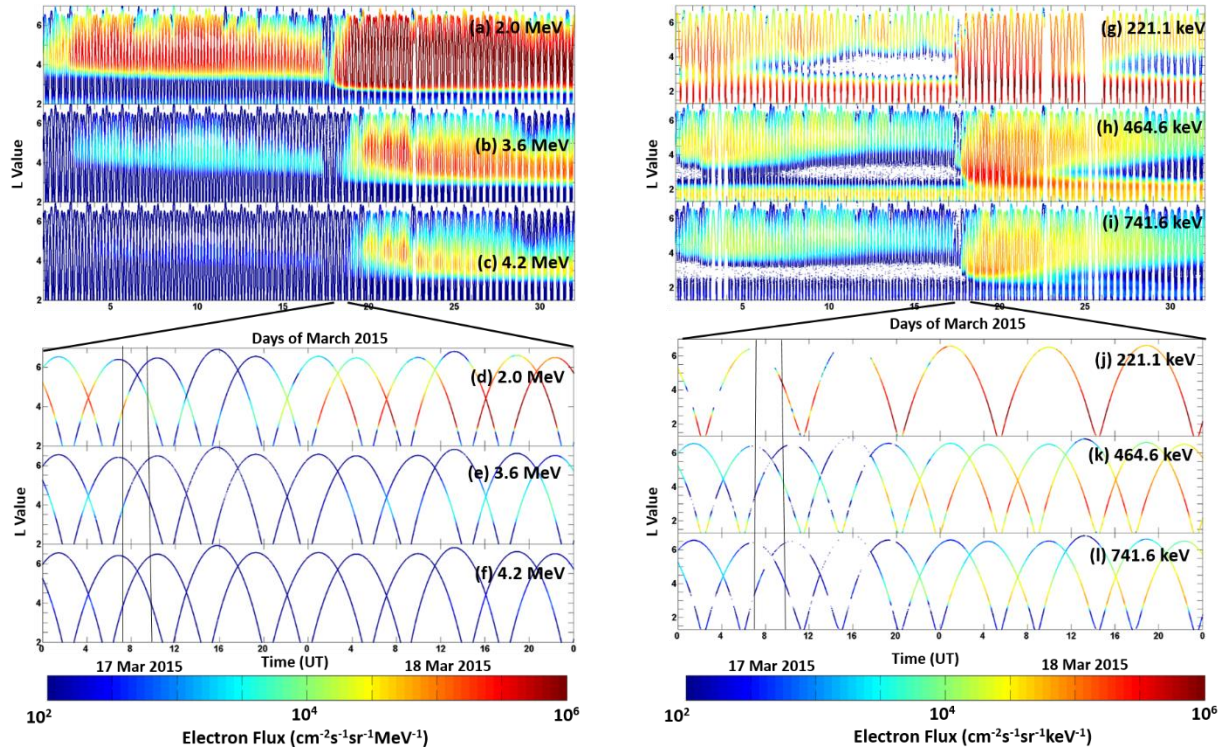


840
841 **Figure 2.** Locations of VLF transmitters, NAA and NML and receivers Seattle (SEA) and St.
842 John's (STJ) respectively along with great circle paths and $L = 3, 4, 5$ contours. The magenta and
843 green dots represent the ionospheric footprints of RBSP-A and RBSP-B at $t_1 = 6:30$ UT and $t_2 =$
844 $8:30$ UT respectively.



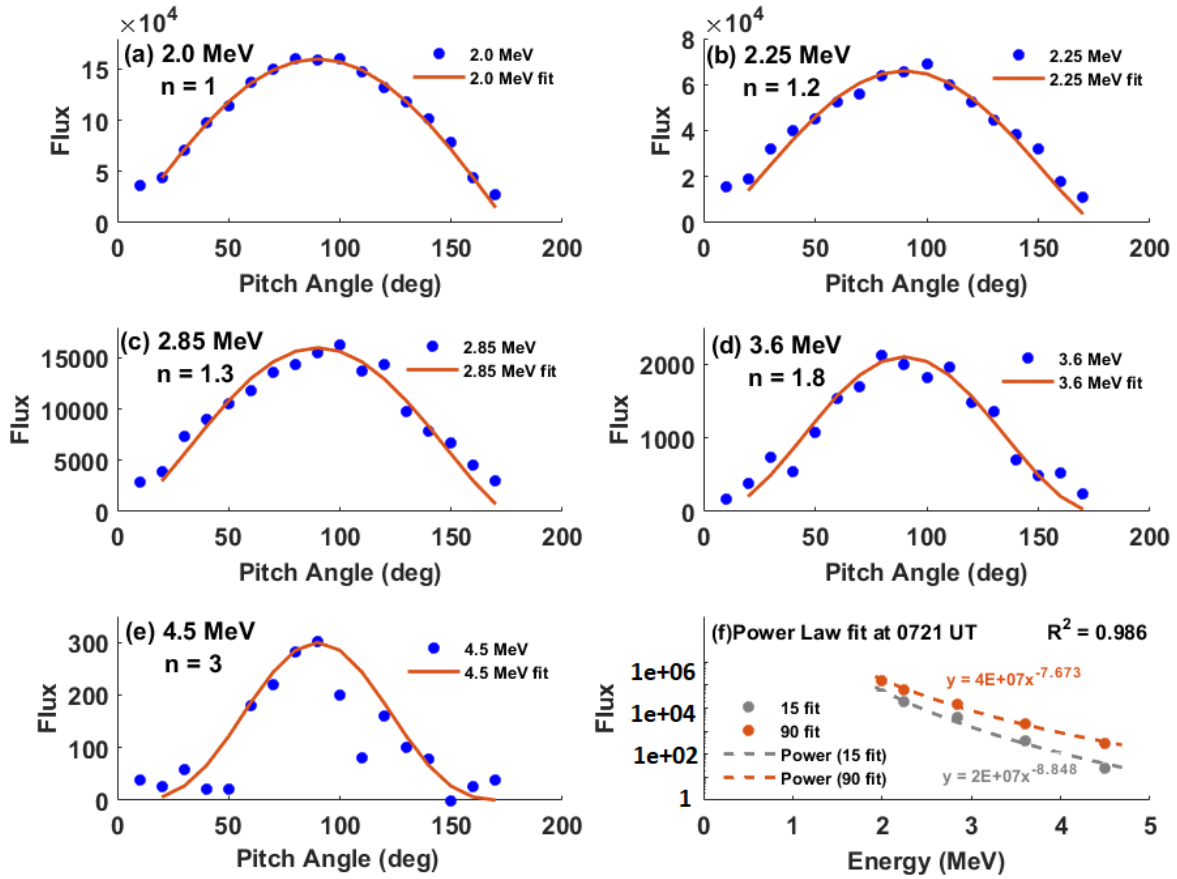
845

846 **Figure 3.** POES P6 trapped (90-deg) and BLC (0-deg) fluxes during 17 March 2015. The colour
 847 bar shows the logarithm of the flux (for electron energy >700 keV), while the vertical dotted lines
 848 indicate the start and end times of the dropout event, and the horizontal red lines indicate the L-
 849 shell range of the VLF paths shown in Figure 2.



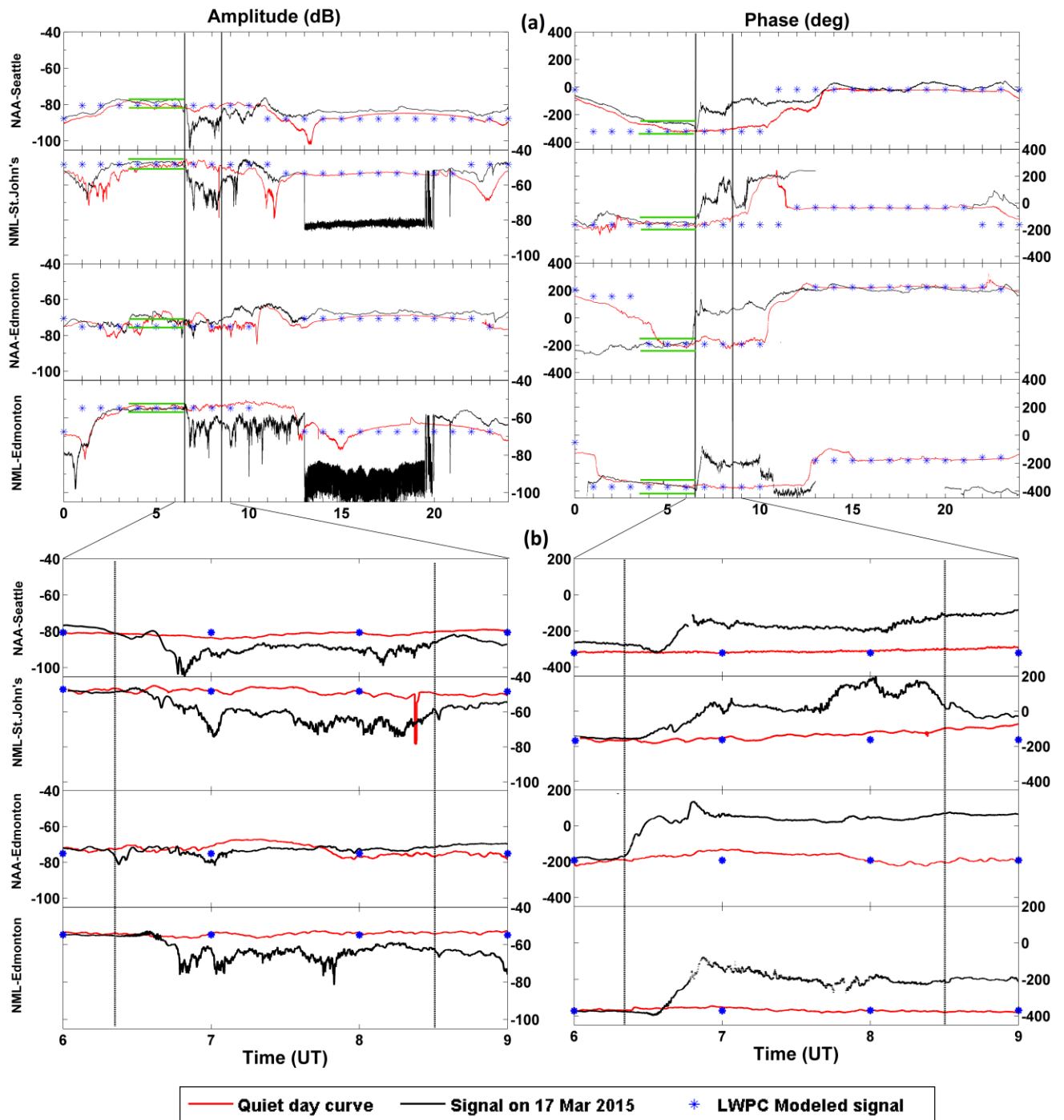
850

851 **Figure 4.** RBSP-B electron flux from Relativistic Electron Proton Telescope (REPT) for (a) 2.0
 852 MeV, (b) 3.6 MeV and (c) 4.2 MeV flux for whole month of March, 2015; (d) 2.0 MeV, (e) 3.6
 853 MeV and (f) 4.2 MeV flux for 17 and 18 March 2015. RBSP-B electron flux from MagEIS for
 854 (g) 226.1 keV, (h) 464.4 keV and (i) 741.6 keV flux for whole month of March, 2015; (j) 226.1
 855 keV, (k) 464.4 keV and (l) 741.6 keV flux for 17 and 18 March 2015. The vertical black lines
 856 represent the duration of VLF perturbations analysed in this study.



857

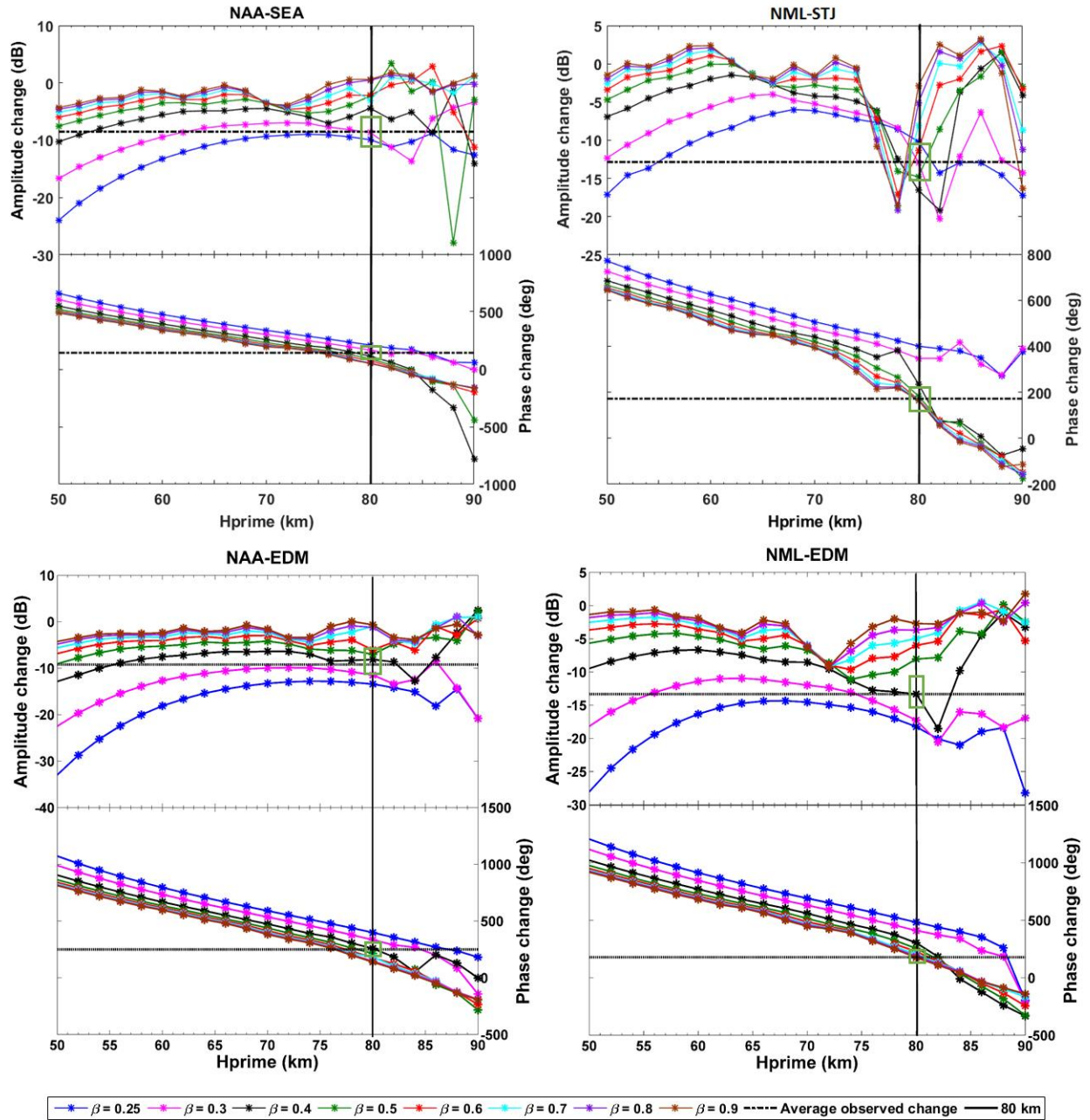
858 **Figure 5.** (panels a –e) RBSP-A pitch angle distributions for a range of relativistic electron
 859 energies at 07:21 UT at L=4 on 17 March 2015. Labels indicate the n parameter fit (using $\sin^n \alpha$)
 860 to the observations. Panel f shows the power law energy spectrum at 90° and 15° pitch angles.



861

862 **Figure 6.** VLF amplitude (left hand column) and phase (right hand column) for the four paths
 863 studied (black lines). Panels (a) show the data for 0-24 UT on 17 March 2015. Panels (b) show
 864 the 6-9 UT period in more detail. Each individual path is identified on the left hand side of the

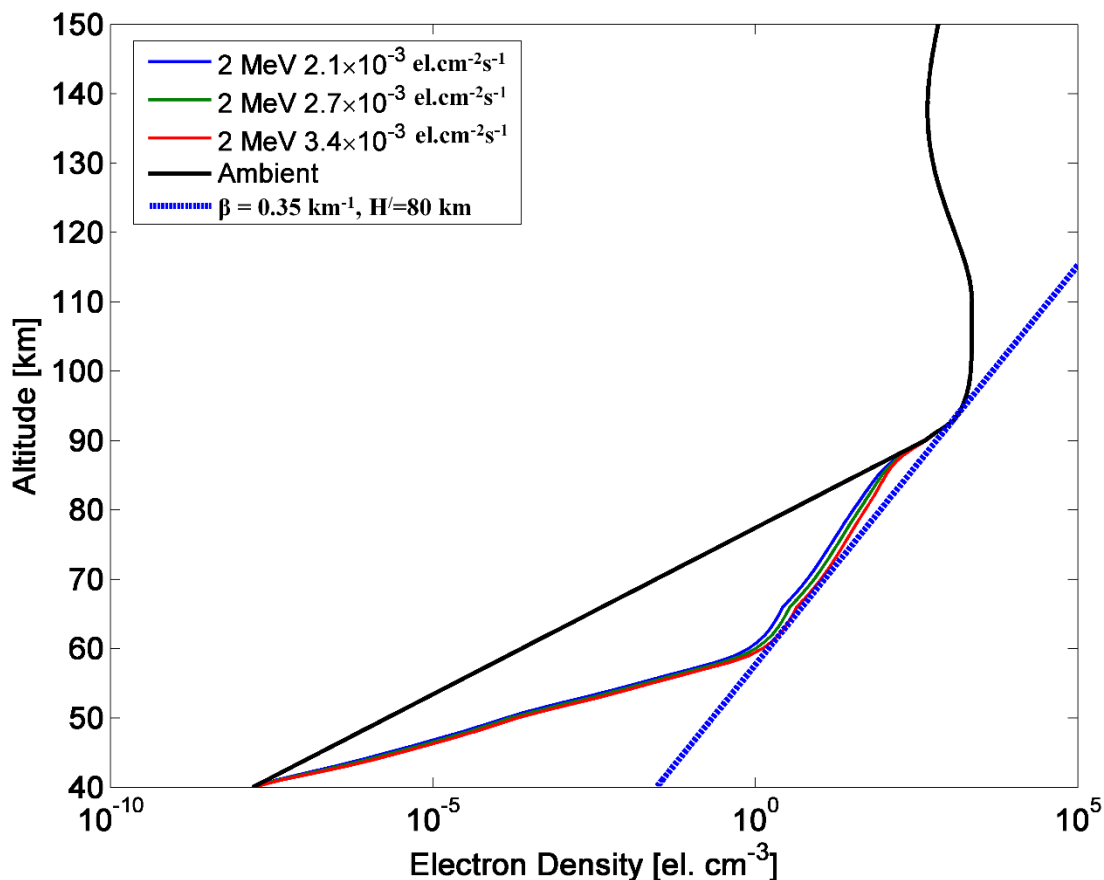
865 row. The red curves represent the signal observed on a representative non-disturbed day (marked
866 as the "Quiet Day Curve" (QDC)). Here the blue asterisks show the results of the LWPC
867 modelling to reproduce the undisturbed QDC observations. Vertical black lines represent the
868 duration over which average of the signal is taken. Horizontal green lines in panels (a) represent
869 an estimate of the uncertainty in the pre-event amplitude and phase levels for 3 hours prior to the
870 start time. See text for more details.



871

872 **Figure 7.** Variation of the LWPC modelled amplitude and phase of VLF signals as a function of
 873 the reference height (H') for varying sharpness factor (β) for the paths: NAA-SEA, NAA-EDM,
 874 NML-STJ, and NML-EDM. Observed perturbation levels on each path are indicated by
 875 horizontal dot-dashed lines, while the inferred H' solution is shown by a vertical line. The green

876 boxes indicate the uncertainty in perturbation level, and thus the H' solution due to uncertainty in
877 the initial QDC levels. See text for more details.



878
879 **Figure 8.** D-region electron number density profiles during the dropout event of 17 March 2015.
880 The black line represents the ambient nighttime profile, while the heavy dashed blue line is the
881 disturbed Wait ionosphere ($\beta=0.35$, $H'=80$ km) inferred from the VLF observations. Lighter blue,
882 green, red lines are the best fitting electron densities profiles produced by the EEP modelling
883 determined from Van Allen Probes data for different flux levels.